Draft version March 31, 2020
Typeset using LaTeX **twocolumn** style in AASTeX63

The Evolution of Rotation and Magnetic Activity in 94 Aqr from Asteroseismology with TESS

Travis S. Metcalfe,[1, 2, 3] Thierry Appourchaux,[4] Sarbani Basu,[5] Derek Buzasi,[6] William J. Chaplin,[7, 8]
Ricky Egeland,[9] Patrick Gaulme,[3, 10] Daniel Huber,[11] Timo Reinhold,[3] Hannah Schunker,[3] Keivan G. Stassun,[12]
Jennifer L. van Saders,[11] Warrick H. Ball,[7, 8] Timothy R. Bedding,[13, 8] Zeynep Çelik,[14] Sébastien Deheuvels,[15]
Rafael A. Garcia,[16, 17] Rasmus Handberg,[8] Tanda Li,[13, 8, 18] Mikkel N. Lund,[8] Antonio J. Mancebo,[19]
Savita Mathur,[19, 20] Benoit Mosser,[21] Martin B. Nielsen,[7, 8, 22] Anthony Noll,[15] Sibel Örtel,[14]
Angela R. G. Santos,[1] Timothy R. White,[13, 8] Mutlu Yildiz,[14] Sallie Baliunas,[23] and Willie Soon[23]

[1] Space Science Institute, 4765 Walnut St., Suite B, Boulder, CO 80301, USA
[2] White Dwarf Research Corporation, 3265 Foundry Pl., Unit 101, Boulder, CO 80301, USA
[3] Max-Planck-Institut für Sonnensystemforschung, Justus-von-Liebig-Weg 3, 37077, Göttingen, Germany
[4] Institut d'Astrophysique Spatiale, UMR8617, Bâtiment 121, 91045 Orsay Cedex, France
[5] Department of Astronomy, Yale University, PO Box 208101, New Haven, CT 06520-8101, USA
[6] Department of Chemistry and Physics, Florida Gulf Coast University, 10501 FGCU Blvd S, Fort Myers, FL 33965
[7] School of Physics & Astronomy, University of Birmingham, Edgbaston, Birmingham B15 2TT, UK
[8] Stellar Astrophysics Centre, Aarhus University, Ny Munkegade 120, DK-8000 Aarhus C, Denmark
[9] High Altitude Observatory, National Center for Atmospheric Research, P.O. Box 3000, Boulder, CO 80307-3000, USA
[10] Department of Astronomy, New Mexico State University, P.O. Box 30001, MSC 4500, Las Cruces, NM 88003-8001, USA
[11] Institute for Astronomy, University of Hawai'i, 2680 Woodlawn Drive, Honolulu, HI 96822, USA
[12] Vanderbilt University, Department of Physics & Astronomy, 6301 Stevenson Center Lane, Nashville, TN 37235, USA
[13] Sydney Institute for Astronomy, School of Physics, University of Sydney 2006, Australia
[14] Department of Astronomy and Space Sciences, Science Faculty, Ege University, 35100 Bornova, İzmir, Turkey
[15] IRAP, Université de Toulouse, CNRS, CNES, UPS, Toulouse, France
[16] IRFU, CEA, Université Paris-Saclay, F-91191 Gif-sur-Yvette, France
[17] AIM, CEA, CNRS, Université Paris-Saclay, Université Paris Diderot, Sorbonne Paris Cité, F-91191 Gif-sur-Yvette, France
[18] Key Laboratory of Solar Activity, National Astronomical Observatories, Chinese Academy of Science, Beijing 100012, China
[19] Instituto de Astrofísica de Canarias, La Laguna, Tenerife, Spain
[20] Dpto. de Astrofísica, Universidad de La Laguna, La Laguna, Tenerife, Spain
[21] LESIA, Observatoire de Paris, Université PSL, CNRS, Sorbonne Université, Université de Paris, 92195 Meudon, France
[22] Center for Space Science, NYUAD Institute, New York University Abu Dhabi, PO Box 129188, Abu Dhabi, United Arab Emirates
[23] Harvard-Smithsonian Center for Astrophysics, Cambridge, MA 02138, USA

ABSTRACT

Most previous efforts to calibrate how rotation and magnetic activity depend on stellar age and mass have relied on observations of clusters, where isochrones from stellar evolution models are used to determine the properties of the ensemble. Asteroseismology employs similar models to measure the properties of an individual star by matching its normal modes of oscillation, yielding the stellar age and mass with much higher precision. We use 27 days of photometry from the *Transiting Exoplanet Survey Satellite* (TESS) to characterize solar-like oscillations in the G8 subgiant of the 94 Aqr triple system. The resulting stellar properties, when combined with a reanalysis of 35 years of activity measurements from the Mount Wilson HK project, allow us to probe the evolution of rotation and magnetic activity in the system. The derived age agrees with gyrochronology for the resolved K2 dwarf secondary, but the rotation period of the subgiant is much shorter than expected from standard models of angular momentum evolution. We conclude that non-standard spin-down is required to explain the stellar properties, and that evolved subgiants in the hydrogen shell-burning phase can reinvigorate large-scale dynamo action and briefly sustain magnetic activity cycles before ascending the red giant branch.

Keywords: Stellar activity; Stellar evolution; Stellar oscillations; Stellar rotation

1. INTRODUCTION

Studies of long-term magnetic variability in solar-type stars rely on measurements of chromospheric activity obtained over many decades. Fortunately, the collection of such observations started in the late 1960s from the Mount Wilson Observatory (Wilson 1978) and continued for more than 35 years. A similar program at Lowell Observatory (Hall et al. 2007) began in the early 1990s and is still ongoing, with the composite time-series for some stars now approaching half a century (Egeland 2017). With sufficiently frequent sampling during each observing season, the modulation from individual active regions can reveal the stellar rotation period (Baliunas et al. 1983), while changes between seasons can constrain latitudinal differential rotation from the slow migration of active regions through the magnetic cycle (Donahue et al. 1996). Such long-term data sets have provided high quality snapshots of magnetic variability in dozens of solar-type stars (Böhm-Vitense 2007; Brandenburg et al. 2017), but the evolutionary thread that connects them is difficult to establish due to uncertainties in the basic stellar properties such as mass and age (Metcalfe & van Saders 2017).

Asteroseismology with the *Transiting Exoplanet Survey Satellite* (TESS, Ricker et al. 2014) is poised to revolutionize our understanding of the evolution of magnetic variability in solar-type stars. Nearly uninterrupted time-series photometry with a 2-minute cadence spanning at least 27 days is sufficient to detect solar-like oscillations in many F- and G-type dwarfs and subgiants down to V$\sim$7 (Campante et al. 2016). The detection of global oscillation properties such as the frequency of maximum oscillation power ($\nu_{\rm max}$) and the mean frequency spacing between consecutive radial overtones ($\Delta\nu$), when combined with spectroscopic properties such as the effective temperature and metallicity ($T_{\rm eff}$, [Fe/H]), can typically determine the stellar mass with an uncertainty of 6% and the stellar age within about 20% (Serenelli et al. 2017). The identification of individual oscillation frequencies can cut these uncertainties in half (Creevey et al. 2017), and even larger improvements in the age precision are possible for subgiants that exhibit mixed-modes, which couple gravity-driven g mode oscillations in the stellar core with pressure-driven p mode oscillations in the envelope (Metcalfe et al. 2010; Deheuvels & Michel 2011).

In this paper, we demonstrate the power of combining ground-based magnetic variability data with asteroseismic measurements of basic stellar properties from TESS. Our initial application is to the 94 Aqr triple system, which includes a blended primary consisting of a G8 subgiant (Aa) and a K3 dwarf (Ab) in a 6-year orbit, and a resolved secondary K2 dwarf (B) separated by 13 arcseconds (Fuhrmann 2008). In Section 2 we provide an overview of the observations, and in Section 3 we reanalyze the archive of chromospheric activity measurements from the Mount Wilson survey (Baliunas et al. 1995) for both the blended primary (A) and the resolved secondary (B) to determine the rotation and activity cycle periods of 94 Aqr Aa and B. All three components are blended in the TESS observations, but the subgiant produces the only detectable asteroseismic signal because the K dwarfs oscillate with a much lower amplitude and higher frequency. In Section 4 we analyze and model the subgiant oscillations to determine the basic stellar properties from asteroseismology, and in Section 5 we establish the accuracy of these results with independent estimates of the subgiant radius and mass, as well as the age of the system. In Section 6 we combine the rotation period from Mount Wilson data with the stellar mass and age from TESS to model the angular momentum evolution of the subgiant, demonstrating that weakened magnetic braking (van Saders et al. 2016) is required to explain the current rotation period. Finally, in Section 7 we discuss our conclusions, including the possibility that evolved subgiants can sustain a “born-again” dynamo before ascending the red giant branch.

2. OBSERVATIONS

2.1. *Mount Wilson HK data*

We use observations from the Mount Wilson Observatory (MWO) HK project (Wilson 1978; Vaughan et al. 1978; Baliunas et al. 1995) to study the short- and long-term variability of magnetic activity in 94 Aqr Aa and B. The HK Project HKP-1 (1966–1978) and HKP-2 (1978–2003) spectrophotometers obtained counts through 1 Å triangular bandpasses centered on the Ca II H & K (hereafter HK) line cores at 3968.470 Å and 3933.664 Å, respectively, as well as two 20 Å pseudo-continuum bands, R centered at 4001.067 Å, and V centered at 3901.068 Å (Vaughan et al. 1978). Emission in the HK line cores has long been known to be a signature of surface magnetic flux (see Linsky & Avrett 1970, for a review), and the disk-integrated HK emission from the Sun reveals the solar cycle (e.g. White & Livingston 1981; Egeland et al. 2017). The ratio of core to pseudo-continuum counts, $S = \alpha_{\rm MWO}(N_H + N_K)/(N_R + N_V)$, where $\alpha_{\rm MWO}$ is a calibration factor, defines the now-standard S-index of magnetic activity. The pair 94 Aqr Aa and Ab were not resolved in the MWO observations, so the 94 Aqr A time series represents the sum of surface fluxes from these components. However, the G8 subgiant contributes approximately 97% of the flux in the relevant bandpasses (see Section 5.1).

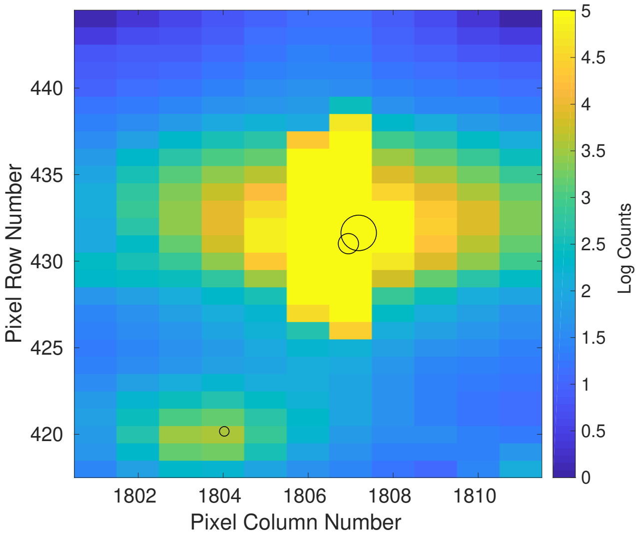

Figure 1. The mean TESS postage stamp for 94 Aqr, averaged over all cadences. Counts are shown on a logarithmic scale to allow visibility of the full count range, and the overlying circles indicate stellar locations from Gaia DR2, with a limiting G magnitude of 14. Blending of the A and B components is apparent.

2.2. *TESS Photometry*

TESS observed 94 Aqr in 2-minute cadence for 27 days during Sector 2 of Cycle 1. We used the target pixel files produced by the TESS Science Processing Operations Center (Jenkins et al. 2016) to produce light curves. A preliminary detection of solar-like oscillations was made with a light curve produced using simple aperture photometry, selecting all pixels with flux above three times the median absolute deviation of a median stacked image over the full observing sector. The final light curve was produced using the photometry pipeline[1] (Handberg et al., in prep.) maintained by the TESS Asteroseismic Science Operations Center (TASOC, Lund et al. 2017), which is based on software originally developed to generate light curves from data collected by the *K2* mission (Lund et al. 2015).

Figure 1 shows the postage stamp for 94 Aqr. The large TESS pixels mean that the components of the 94 Aqr system are separated by less than one pixel on the detector. However, we made an effort to extract separate light curves for the two components. We built custom aperture masks around well-separated portions of the combined stellar image, conducted photometric extractions using those masks, and detrended the resulting light curves against spacecraft pointing data using a second-order two-dimensional polynomial fit, which has worked well for *Kepler* data in the past (Buzasi et al. 2015). Our goal was to construct aperture masks which were dominated by the wings of the images of the two stars, which might then allow us to successfully separate the light curves. Despite our detrending efforts, light curves resulting from such aperture masks tend to be dominated by photometric jitter resulting from spacecraft motion, and we were unable to unequivocally separate the target light curves using this approach.

2.3. *Derived Luminosity*

We derived an updated luminosity for 94 Aqr Aa from speckle observations of the close ($0\farcs15$) binary A component and the Gaia DR2 parallax of the resolved B component (see Section 5.2). The total V magnitude of the A component is 5.18 ± 0.01 (Fabricius et al. 2002), while the magnitude difference between Aa and Ab from speckle imaging is 3.1 (Tokovinin et al. 2015). The bolometric correction (-0.04) was deduced from an extrapolation of Figure 26 in VandenBerg & Clem (2003), adopting $T_{\rm eff} = 5461 \pm 40$ K from Gray et al. (2006), the parallax of 94 Aqr B adjusted for a small systematic offset (e.g., Stassun & Torres 2018; Zinn 2019), and interstellar extinction $A_V = 0.02^{+0.07}_{-0.02}$ (see Section 5.1). The luminosity deduced from these parameters is $L = 3.31^{+0.22}_{-0.07}\ L_\odot$.

3. ROTATION AND ACTIVITY CYCLES

The resolved components of the 94 Aqr system (A and B) were observed by the Mount Wilson program during the years 1967–2003. The S-index was measured during annual observing seasons covering time spans between two and six months. Each observing season shows large variability, which is attributed to active regions rotating in and out of view. Baliunas et al. (1996) measured rotation periods of 42 days and 43 days for the A and B components, respectively. Using these periods as initial guesses, we fit a sinusoid to the data to obtain a rotation period for each observing season. We also computed the generalized Lomb-Scargle periodogram (Zechmeister & Kürster 2009) for each season and compared the derived periods to the peaks in the periodogram. The periodogram was normalized to unity, i.e. peak heights $h_{\rm peak}$ close to one indicate strong periodicity, and small peak heights close to zero indicate irregular variability. The peak heights at the derived periods were used to estimate the rotation period uncertainties. We followed the relation $\sigma(f) = \sqrt{6/N} \cdot \sigma(m)/(\pi T a)$ given in Montgomery & O'Donoghue (1999). We computed the root-mean-square deviation $\sigma(m) = \sqrt{\sigma^2 \cdot (1 - h_{peak})}$, where σ^2 is the variance of the zero mean time series, and $h_{\rm peak}$ is the normalized peak height at the derived period. The

---

[1] https://tasoc.dk/code/

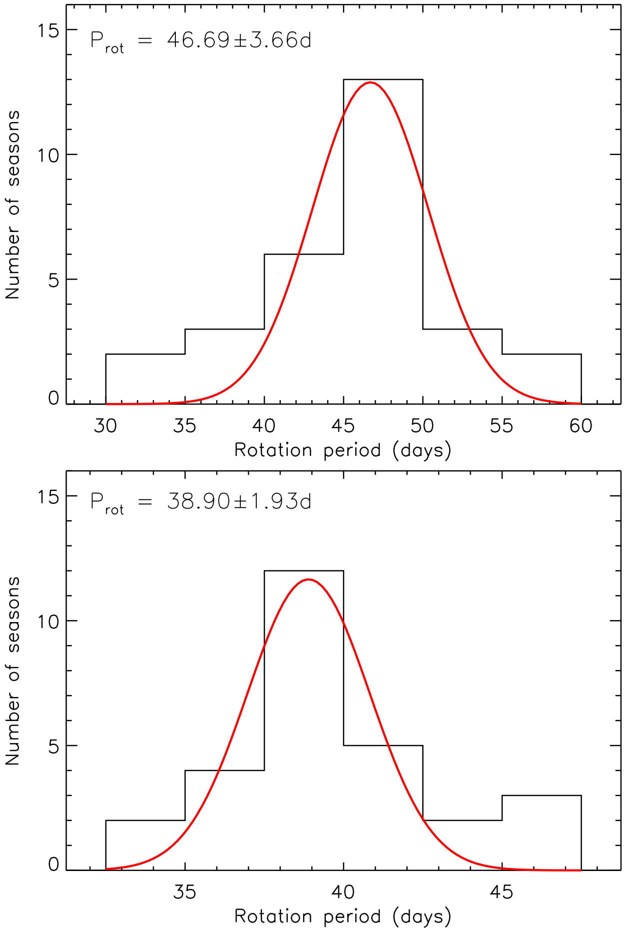

Figure 2. Distribution of seasonal rotation period measurements for 94 Aqr Aa (top) and 94 Aqr B (bottom) from the Mount Wilson S-index data. The reported rotation period and uncertainty correspond to the mean and standard deviation of a Gaussian fit (red curves) to each distribution.

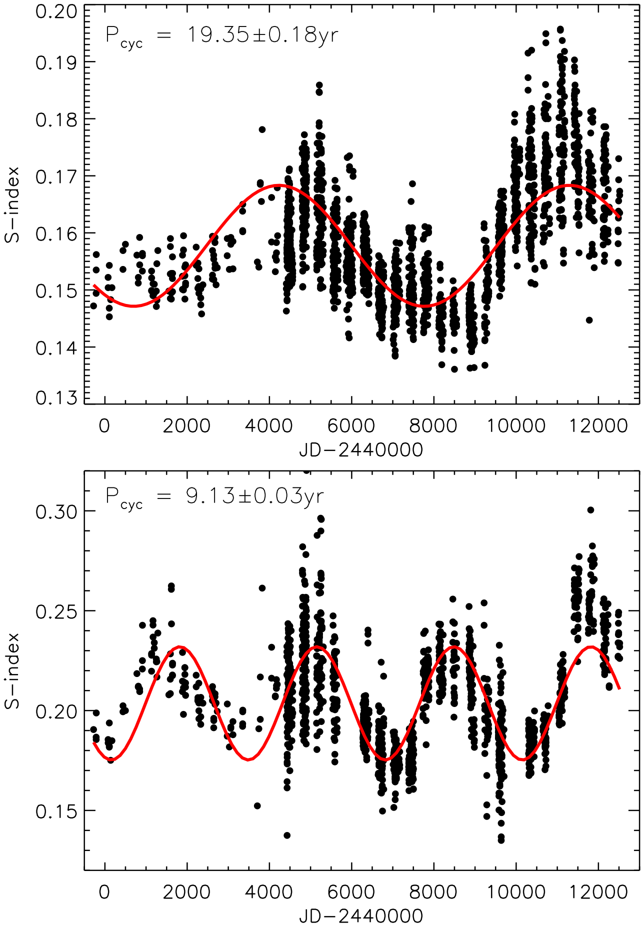

Figure 3. Long-term variability of 94 Aqr Aa (top) and 94 Aqr B (bottom) from the Mount Wilson S-index data. The reported activity cycle period and uncertainty come from fitting a sinusoid (red curves) to each time series.

rotation period distribution for each component is shown in Figure 2. We fit a Gaussian to the rotation period distribution and report the mean and standard deviation as the rotation period and uncertainty for each component.

In addition to the rotational variability, each S-index time series shows long-term variability due to magnetic activity cycles. We computed the Lomb-Scargle periodogram of the of the full S-index time series for each component to search for the activity cycle period. A sinusoid was fit to the data using the highest periodogram peak as the initial period guess, and the uncertainties were estimated as described above. The activity cycles from the S-index time series are evident for both components (see Figure 3).

For the resolved B component, the rotation and activity cycle periods can be attributed unambiguously to the K2 dwarf. For the blended A component, the G8 subgiant (Aa) contributes approximately 97% of the flux in the relevant bandpasses (see Section 5.1). Consequently, the 3% of the flux contributed by the K3 dwarf (Ab) would need to vary by roughly an order of magnitude to explain the observed S-index variation of up to 30% on both rotational and activity cycle timescales. Such modulations would be unprecedented (e.g., see Soon et al. 1994), so we identify the G8 subgiant as the source of the S-index variability. The differences between the rotation and activity cycle periods of the resolved components also supports this interpretation, because the K dwarfs in the system are otherwise very similar. The implications of the observed activity cycle, and the possibility of a "born-again" dynamo in evolved subgiants, are discussed in Section 7.

4. ASTEROSEISMOLOGY OF 94 Aqr Aa

4.1. *Extracting the oscillation parameters*

We compute the power spectral density (PSD) of the TESS light curve (see Section 2.2) to analyze the stel-

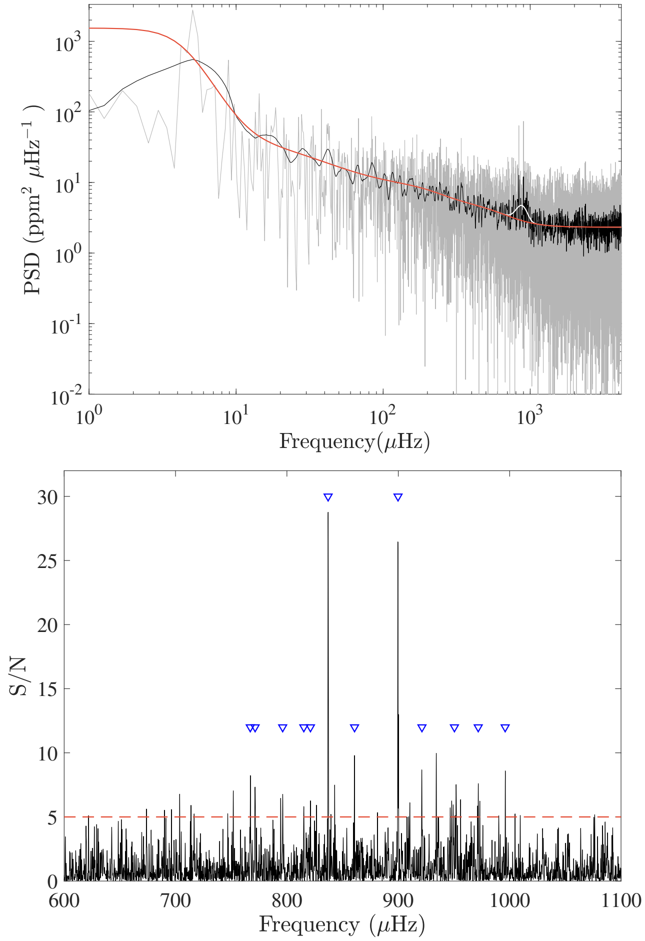

Figure 4. Top: power spectral density (PSD) of the TESS light curve as a function of frequency in μHz. The red line represents the fit to the background noise, and the white line includes the excess power due to oscillations. Bottom: ratio of the power spectrum to the background noise as a function of frequency in the range where oscillation modes are detected. Within this frequency interval, peaks above the red line have $< 1\%$ probability of being due to noise.

lar oscillations. Because the signal to noise ratio (S/N) of the oscillations is relatively low, six teams analyzed the oscillation spectrum to agree on a frequency set. The frequency analysis involves taking into account the background noise caused by surface granulation (e.g., Harvey et al. 1988), then extracting the star's eigenmodes (see Figure 4). Because we are dealing with a subgiant star, the latter involves considering mixed dipolar modes, where $l = 1$ p modes excited in the convective envelope couple with g modes from the core.

The computation of mixed modes is based upon Mosser et al. (2015). We first assume that the frequencies of radial modes $\nu_{n_p,0}$ are given by:

$$\nu_{n_p,0} = \left[n_p + \epsilon + \frac{\alpha}{2}(n_p - n_{\max})^2\right]\Delta\nu \tag{1}$$

where n_p is the radial order, ϵ is a phase offset, α is the mean curvature of the $l = 0$ pattern as a function of frequency, $n_{\max}$ is the closest radial order to $\nu_{\max}$, and $\Delta\nu$ is the mean large frequency separation between consecutive radial overtones. The frequencies of the dipolar ($l = 1$) p modes are given by:

$$\nu_{n_p,1} = \nu_{n_p,0} + \left(\frac{1}{2} - d_{01}\right)\Delta\nu \tag{2}$$

where d_{01} is the mean separation in between $l = 0$ and $l = 1$ modes of a given order n, relative to $\Delta\nu$. The periods of dipolar g modes $P_{n_g,1}$ are given by:

$$P_{n_g,1} = (n_g + \alpha_1)\Delta\Pi_1 \tag{3}$$

where n_g is the g mode order, α_1 is a constant and $\Delta\Pi_1$ is the period spacing of dipolar modes.

By definition, a mixed mode has a dual character of being a p mode and a g mode. The solution of the continuity equation by Shibahashi (1979) led to an implicit expression for the mixed mode frequency ν_{pg} as:

$$\tan\theta_p = q\tan\theta_g \tag{4}$$

where θ_p and θ_g are the phase functions of ν_{pg} with respect to the p mode and g mode frequencies, and q is the coupling factor. The phase function θ_p is given by:

$$\theta_p = \pi\frac{(\nu_{pg} - \nu_{n_p,1})}{\Delta\nu(n_p)} \tag{5}$$

where

$$\Delta\nu(n_p) = [1 + \alpha(n_p - n_{\max})]\,\Delta\nu \tag{6}$$

and θ_g is given by:

$$\theta_g = \pi\frac{1}{P_1}\left(\frac{1}{\nu_{pg}} - \frac{1}{\nu_{n_g,1}}\right). \tag{7}$$

When there is no coupling, $q = 0$ and there are no mixed modes, so $\nu_{pg} = \nu_{n_p,1}$. Otherwise, the solutions to Eq. (4) provide the frequencies of the mixed modes.

The observed oscillation spectrum is typical of a subgiant star, where all $l = 1$ modes are of mixed nature, leading to the impression of an irregular mode distribution as a function of frequency. For this reason, the determination of $\Delta\nu$ was initially ambiguous, with estimates ranging from about 40 to 60 μHz. We converged to a value of $\Delta\nu = 50.2 \pm 0.4$ μHz. Similarly, because of the rather low S/N, our estimate of the frequency of maximum oscillation power suffers from a relatively large uncertainty at $\nu_{\max} = 875 \pm 12$ μHz.

From a consensus of the individual teams, we identify four radial (l=0), five dipole (l=1), and two quadrupole (l=2) modes that are above our significance threshold

Table 1. Identified Oscillation Frequencies.

n	l	$\nu_{nl}^{\rm obs}$ (μHz)	$\nu_{nl}^{\rm mod}$ (μHz)	$\nu_{nl}^{\rm cor}$ (μHz)
15	0	771.39 ± 0.19	773.63	771.32
16	0	821.62 ± 2.85	826.39	821.73
18	0	921.29 ± 0.23	933.78	921.93
19	0	971.64 ± 0.29	987.71	970.81
15	1	794.37 ± 0.14	801.01	797.96
16	1	837.02 ± 0.12	839.83	837.48
16	1	860.61 ± 0.14	862.92	858.32
17	1	899.76 ± 0.17	909.41	900.14
18	1	950.49 ± 1.21	960.71	947.10
19	1	996.11 ± 0.15	1010.47	994.33
14	2	767.21 ± 0.31	768.71	766.60
15	2	815.28 ± 0.15	821.81	817.46

(S/N $\geq$ 5). The identified frequencies are listed in Table 1 and marked with blue triangles in the bottom panel of Figure 4. The two sets of closely-spaced triangles at the lower end of the frequency range are pairs of l=2 and l=0 modes, while the two largest peaks are mixed l=1 modes. Slightly below the frequency range with identified modes, there are a few marginal peaks that may be additional l=1 and l=2 modes for which we did not reach a consensus. Finally, there are three peaks above our significance threshold that remain unidentified: a relatively strong peak near 935 μHz, a weaker peak adjacent to a mixed mode near 843 μHz, and a marginal peak close to an l=2/l=0 pair at 826 μHz. Future TESS observations may help to clarify these ambiguities.

4.2. *Modeling the oscillation modes*

Several teams attempted to match the observed oscillation frequencies identified above, using stellar evolution models from MESA (Paxton et al. 2011), ASTEC (Christensen-Dalsgaard 2008), and the Yale Rotating Evolution Code (YREC, Demarque et al. 2008) in its non-rotating configuration. We found reasonable agreement between the resulting determinations of asteroseismic radius, mass, and age. For consistency with our subsequent analysis of the angular momentum evolution (see Section 6), below we provide details only for the results obtained with YREC.

We initially constructed a grid of models with masses in the range 1.17 $M_\odot$ to 1.25 $M_\odot$ with a spacing of 0.01 $M_\odot$. For each mass, models were created with five values of the mixing length parameter spanning $\alpha_{\rm MLT}$ = 1.5 to 2.3, initial helium abundances from the primordial helium abundance of 0.248 (Steigman 2010) to 0.30 in steps of 0.01, and initial [Fe/H] in the range +0.22 to +0.33 in steps of 0.01. We use the Grevesse & Sauval (1998) solar mixture to convert [Fe/H] to Z/X. For each of the parameters, the models were evolved from the zero-age main-sequence (ZAMS) to an age of 11 Gyr. Models were output at intermediate ages.

The models were constructed using OPAL opacities (Iglesias & Rogers 1996) supplemented with low temperature opacities from Ferguson et al. (2005). The OPAL equation of state (Rogers & Nayfonov 2002) was used. All nuclear reaction rates are obtained from Adelberger et al. (1998), except for that of the $^{14}N(p,\gamma)^{15}O$ reaction, which we adopt from Formicola et al. (2004). All models included gravitational settling of helium and heavy elements using the formulation of Thoul et al. (1994). The oscillation frequencies of the models were calculated with the code of Antia & Basu (1994).

The fits to the observations were done in two steps: we first looked for models that provided a good match to the frequencies of the l=0 and l=2 modes, in addition to showing consistency with the observed luminosity ($L = 3.31^{+0.22}_{-0.07}\ L_\odot$), $T_{\rm eff}$ and [Fe/H] (Gray et al. 2006).

The quality of the fit was defined as follows. For each observable, $T_{\rm eff}$, [Fe/H] and luminosity L, we define a likelihood. For instance, the likelihood for effective temperature was defined as

$$\mathcal{L}(T_{\rm eff}) = D\exp(-\chi^2(T_{\rm eff})/2), \tag{8}$$

with

$$\chi^2(T_{\rm eff}) = \frac{(T_{\rm eff}^{\rm obs} - T_{\rm eff}^{\rm mod})^2}{\sigma_T^2}, \tag{9}$$

where σ_T is the uncertainty on the effective temperature, and D is a normalization constant. We define the likelihoods for [Fe/H] and L in a similar manner.

For the frequencies, we first corrected for surface effects using the two-term surface correction proposed by Ball & Gizon (2014):

$$\delta\nu_{nl} = \nu_{nl}^{\rm obs} - \nu_{nl}^{\rm mod} \tag{10}$$

$$= \frac{1}{I_{nl}}\left[a\left(\frac{\nu_{nl}}{\nu_{\rm ac}}\right)^{-1} + b\left(\frac{\nu_{nl}}{\nu_{\rm ac}}\right)^{3}\right], \tag{11}$$

where $\delta\nu_{nl}$ is the difference in frequency for a mode of degree l and order n between a star and its model, ν_{nl} is the frequency and I_{nl} is the inertia of the mode, and $\nu_{\rm ac}$ is the acoustic cut-off frequency, with coefficients a and b determined from a generalized least-squares fit to the frequency difference of the $l = 0$ modes. This allows us to define a likelihood for frequencies. We define $\nu_{nl}^{\rm cor} = \nu_{nl}^{\rm mod} - S$, where S is defined by the right-hand side of Eq. 11 but now applied to both $l = 0$ and $l = 2$

Table 2. Stellar Properties of 94 Aqr Aa.

	Asteroseismic	Other	Source
Radius ($R_\odot$)	2.06 ± 0.05	2.07 ± 0.03	(1)
Mass ($M_\odot$)	1.22 ± 0.02	1.24 ± 0.08	(2)
Age (Gyr)	6.2 ± 0.4	6.3 ± 0.6	(3)
$T_{\rm eff}$ (K)	5433 ± 43	5461 ± 40	(4)
[Fe/H] (dex)	$+0.21 \pm 0.03$	$+0.23 \pm 0.08$	(4)
Luminosity ($L_\odot$)	3.34 ± 0.07	$3.31^{+0.22}_{-0.07}$	(5)

References—(1) Section 5.1; (2) Section 5.2; (3) Section 5.3; (4) Gray et al. (2006); (5) Section 2.3

modes.

$$\chi^2(\nu) = \frac{(\nu_{nl}^{\rm obs} - \nu_{nl}^{\rm cor})^2}{\sigma_{nl}^{\rm obs}}. \tag{12}$$

Consequently

$$\mathcal{L}(\nu) = C \exp\left(-\frac{\chi^2(\nu)}{2}\right), \tag{13}$$

where C is a normalization constant.

The total likelihood for each model is then

$$\mathcal{L}_{\rm total} = \mathcal{L}(\nu)\mathcal{L}(T_{\rm eff})\mathcal{L}([{\rm Fe/H}])\mathcal{L}(L). \tag{14}$$

The medians of the marginalized likelihoods of the ensemble of models were used to determine the most likely parameters, after converting them to a probability density by normalizing the likelihood by the prior distribution of each parameter.

A finer grid in mass and age was created around the most likely values of these parameters in order to fit the $l = 1$ modes. The likelihoods were calculated again, except that now in Eq. (12) we also used the $l = 1$ modes. The optimal asteroseismic parameters were derived from the new probability density, and they are listed in Table 2 along with independent estimates (see Section 5) and the other available constraints. Note that because we did not use a global optimization technique, it is possible that a better fit to the observations exists.

5. ACCURACY OF THE STELLAR PROPERTIES

5.1. *Radius from SED*

We performed a fit to the broadband catalog photometry of 94 Aqr A in order to make an independent determination of the stellar radius. We follow the procedures described in Stassun & Torres (2016); Stassun et al. (2017, 2018). Briefly, we adopted the best available spectroscopic values for $T_{\rm eff}$ and [Fe/H], and then fit a standard stellar atmosphere model (Kurucz 1992) to the broadband spectral energy distribution (SED) in order to determine empirically the bolometric flux at Earth ($F_{\rm bol}$). The free parameter of the fit is the interstellar extinction. Using the Gaia DR2 parallax, adjusted for the known small systematic offset (e.g., Stassun & Torres 2018; Zinn 2019), the stellar radius is then determined via the Stefan-Boltzmann relation.

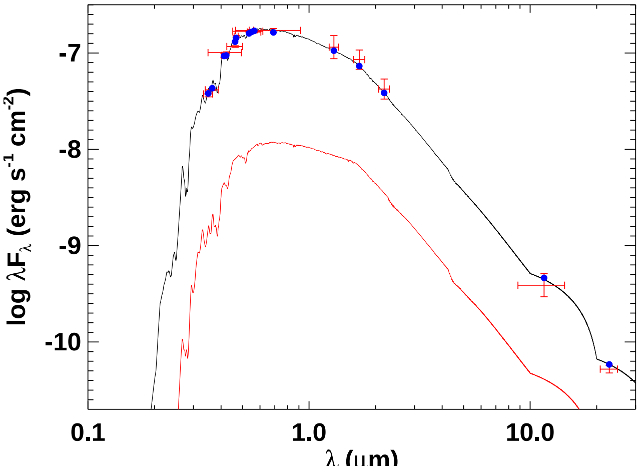

Figure 5. Spectral energy distribution (SED) fit to the broadband photometry of 94 Aqr A. The fit to 94 Aqr Aa is shown in black, with observed fluxes as red symbols and passband integrated model fluxes as blue symbols. The red curve shows the SED of the companion (Ab), which is used to correct for light contamination in the SED of 94 Aqr Aa.

We pulled the Johnson UBV magnitudes from the Mermilliod (2006) homogenized photometric catalog of bright stars, the $B_T V_T$ magnitudes from *Tycho-2*, the Strömgren $ubvy$ magnitudes from Paunzen (2015), the JHK_S magnitudes from *2MASS*, the W3–W4 magnitudes from *WISE*, and the G magnitude from *Gaia*. Together, the available photometry spans the full stellar SED over the wavelength range 0.35–22 μm.

We adopted the spectroscopic parameters from Gray et al. (2006): $T_{\rm eff} = 5461 \pm 40$ K[2] and $[{\rm Fe/H}] = +0.23 \pm 0.08$. We also adopted the parameters for the blended Ab component from Docobo et al. (2018), and similarly fit its SED, in order to correct the $F_{\rm bol}$ of 94 Aqr Aa for contamination of light in the broadband photometry from the close companion.

The fit is good (see Figure 5), with reduced $\chi^2 = 3.3$ and an extinction of $A_V = 0.02^{+0.07}_{-0.02}$. The resulting bolometric flux is $F_{\rm bol} = (2.18 \pm 0.25) \times 10^{-7}$ erg s^{-1} cm^{-2}, which with the parallax gives $R_{\rm SED} = 2.07 \pm 0.03\ R_\odot$,

---

[2] Note that the quoted uncertainty on $T_{\rm eff}$ does not account for systematics between different methods and the fundamental $T_{\rm eff}$ scale set by the accuracy of interferometric angular diameters, which can be $\gtrsim 2\%$ (Casagrande et al. 2014; White et al. 2018).

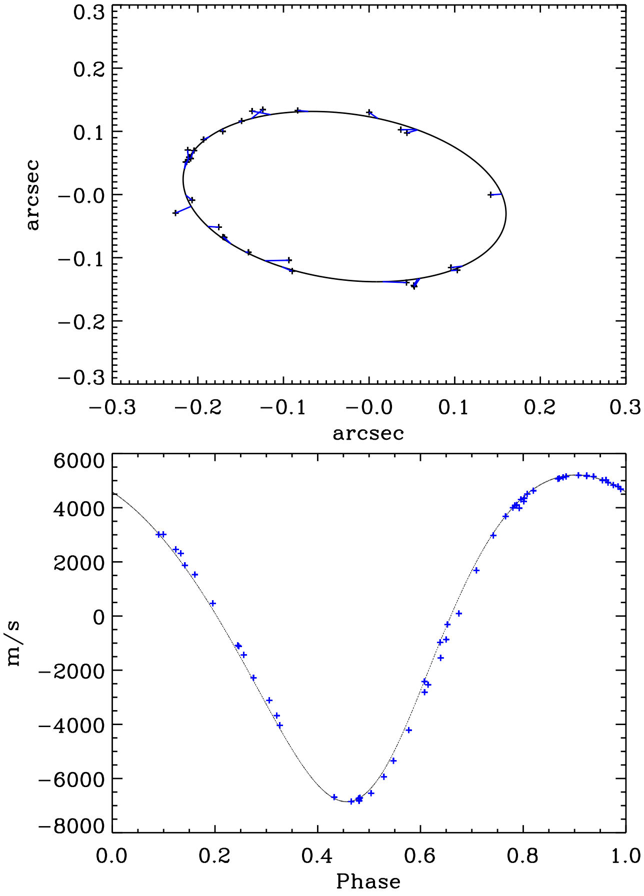

Figure 6. Results of a simultaneous fit to the astrometry (top) and spectroscopy (bottom) of 94 Aqr A. Data are shown with blue points, and the fit is shown in black.

in good agreement with the asteroseismic value ($R = 2.06 \pm 0.05\ R_{\odot}$).

5.2. *Mass from astrometry and spectroscopy*

To derive the individual masses of 94 Aqr Aa and Ab, we used the available data from astrometry and spectroscopy. For astrometry, we used the same data available to Docobo et al. (2018). For spectroscopy, we used radial velocities measured by Sarma (1962) and Katoh et al. (2013). We then jointly fitted the astrometry and spectroscopy data using an MCMC approach as described in Marcadon et al. (2018). The results are illustrated in Figure 6, and the orbital parameters are given in Table 3.

Docobo et al. (2018) used the Gaia parallax for the Aa/Ab system to derive the masses of the two components. Unfortunately the latest Gaia release does not take into account the binarity. This means the parallax of 94 Aqr A is not useful, because the period of the orbit is about 6.3 years. Instead, we use the parallax of 94 Aqr B ($\pi = 44.515 \pm 0.055$ mas, Gaia Collaboration et al. 2018), which has an orbital period around A that is longer than a few hundred years (Mason et al. 2001).

We derive individual masses for Aa and Ab following the same approach as Docobo et al. (2018). The error propagation is done using the MCMC solution, thereby taking into account the intrinsic correlations between the various orbital parameters. We found $M_{\rm Aa} = 1.24 \pm 0.08\,M_{\odot}$, in agreement with the asteroseismic value ($M = 1.22{\pm}0.02\,M_{\odot}$), and $M_{\rm Ab} = 0.81{\pm}0.04\,M_{\odot}$.

Table 3. Orbital Parameters of 94 Aqr A.

Parameter	Value
Period (year)	6.298 ± 0.005
T	2012.310 ± 0.05
e	0.1621 ± 0.0056
a (arcsec)	0.1928 ± 0.0036
i (°)	47.26 ± 1.92
Ω (°)	343.95 ± 1.10
ω (°)	31.50 ± 2.64
K (km s^{-1})	6.030 ± 0.038
π (mas)	44.515 ± 0.055

5.3. *Age from gyrochronology*

Although a relationship between rotation period and stellar age has not yet been calibrated for subgiants, we can estimate an age for the 94 Aqr system by applying the gyrochronology relation of Barnes (2010) to the properties of the K dwarf secondary. Adopting the rotation period determined for 94 Aqr B in Section 3 ($P_{\rm rot} = 38.9{\pm}1.9$ days), and the color $B{-}V = 0.91$ from Baliunas et al. (1996), the gyrochronology relation yields $t_{\rm gyro} = 6.3 \pm 0.6$ Gyr, which agrees well with the age of 94 Aqr Aa from asteroseismology ($t = 6.2 \pm 0.4$ Gyr).

6. ANGULAR MOMENTUM EVOLUTION

We model the angular momentum evolution of 94 Aqr Aa using the braking prescriptions and model grids described in van Saders et al. (2016). We examine two distinct braking prescriptions: the first is a “standard” model (van Saders & Pinsonneault 2013) calibrated to young open clusters and the Sun, and the second is the modified braking model of van Saders et al. (2016), motivated by the inclusion of additional asteroseismic calibrator stars. The van Saders et al. (2016) model adapted the standard braking model to include a critical Rossby number, Ro_{crit} above which magnetic braking does not occur and angular momentum is conserved. Because of this weakened braking, the modified model generally predicts faster rotation periods than the standard model, so we tried both prescriptions.

We model 94 Aqr Aa with a Monte Carlo approach, using `emcee` (Foreman-Mackey et al. 2013). We search in mass, age, and bulk composition ([Z/X]) for models that match a set of observable surface constraints: $T_{\rm eff}$ and [Fe/H] (from spectroscopy), and radius (from asteroseismology). We adopt the asteroseismically determined mass and age as priors, where the prior is assumed to be Gaussian with a width determined by the uncertainty. We use the surface abundance inferred from spectroscopy as a prior on the bulk abundance, again with the assumption of Gaussian priors. A total of 6 chains are run for 100000 steps each, with the first 5000 steps discarded as burn-in. Such a run corresponds to >1000 autocorrelation times in all variables of interest.

We adopt the form of the braking model described in van Saders et al. (2016), with the overall braking normalization $f_K = 6.5749125$, saturation angular velocity $\omega_{crit} = 3.3938561 \times 10^{-5}$ rad/s, initial disk rotation period of $P_{disk} = 8.1343097$ days and disk-locking timescale of $T_{disk} = 0.28098312$ Myr. These parameters correspond to the "fast-launch" conditions in van Saders & Pinsonneault (2013), chosen because: 1) 94 Aqr is old, making the choice of launch conditions unimportant, and 2) we are specifically comparing this standard model to the modified Ro_{crit} prescription that predicts more rapid rotation, and thus the fast-launch case represents the more conservative choice. Our models are assumed to rotate as solid bodies, and there is no feedback on the stellar structure from the rotation. We model the rotational evolution using the `rotevol` code (as in van Saders et al. 2016; Somers & Pinsonneault 2016) atop formally non-rotating YREC stellar evolution tracks. For the modified braking model, we use the same parameters as those in the standard model, but setting $\mathrm{Ro}_{crit} = 1.97$ (van Saders et al. 2019). The stellar model grid physics are the same as described in van Saders & Pinsonneault (2013) with the addition of gravitational settling and diffusion.

The standard braking model predicts a rotation period $P = 78.0^{+6.0}_{-6.5}$ days, while the weakened braking model ($\mathrm{Ro}_{crit} = 1.97$) predicts a period $P = 48.3^{+3.3}_{-3.6}$ days (see Figure 7). Only the weakened braking model agrees with the observed rotation period ($P_{\rm rot} = 46.69 \pm 3.66$ days, see Section 3). This fit uses the radius and $T_{\rm eff}$ as constraints, but the predicted periods are unchanged within the uncertainties if radius and luminosity are used instead. If we assume $\mathrm{Ro}_{crit} = 2.16$ as in van Saders et al. (2016), the predicted period is 53 ± 4 days.

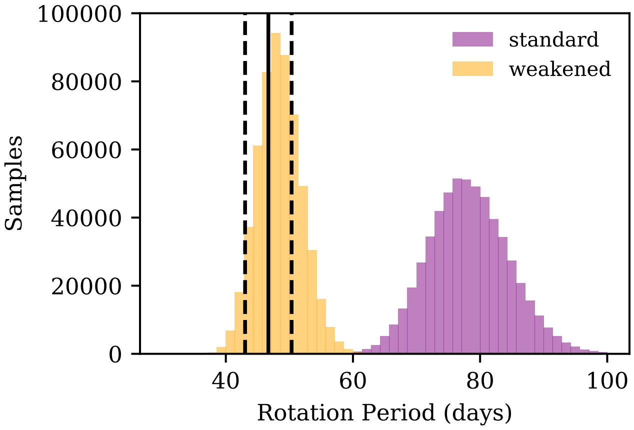

Figure 7. Predictions from a standard spin-down model (purple) and weakened braking model (orange) for the rotation period of 94 Aqr Aa. The observed period is shown as a black line, with 1σ uncertainties shown as dashed lines.

The standard spin-down model has many assumptions, but taking a more sophisticated approach does not ease the tension with the observed rotation period. We have assumed solid-body rotation in our models. While this is a reasonable assumption near the turnoff, stars near the base of the red giant branch display differential rotation with depth (Deheuvels et al. 2014). The van Saders & Pinsonneault (2013) standard braking models predict more rapid surface rotation near the base of the red giant branch than is observed; this is the expected trend when a solid-body model is used to describe a subgiant that is actually differentially rotating with depth. If some form of core-envelope decoupling (e.g. Denissenkov et al. 2010; MacGregor & Brenner 1991) is functioning, the general sense would be to slow down the envelope relative to standard solid-body models, since some of the star's angular momentum will be sequestered in the stellar core. Therefore, core-envelope decoupling would produce a trend *opposite* to the more rapid rotation that we are trying to reproduce.

We have made specific assumptions about the initial rotation period, but stars are born with a range of rotation periods. If we start a star of this mass and metallicity on the ZAMS at critical rotation velocity (a factor of 66 times faster than that assumed in our standard model), it has a period that differs by only a day from our standard braking case by the age of 94 Aqr Aa; a change in initial conditions is insufficient to produce the more rapid observed rotation. If the main-sequence lifetime is prolonged by rotational mixing (which we do not include in our models), it would lengthen the period of time the star has to lose angular momentum, driving the rotation to longer periods rather than shorter.

Rotation velocity is a very strong function of mass, particularly near the Kraft (1967) break, where stars hotter than the break rotate rapidly, while cooler stars rotate more slowly. The dichotomy is the result of the disappearing convective envelopes in more massive stars, and their resulting weak large-scale fields and magnetic braking. We investigated whether the observed rotation of 94 Aqr Aa could simply be the result of an underestimated stellar mass. We added rotation period to the observable constraints, and assumed broad Gaussian priors on mass, age and composition, with 1σ Gaussian prior widths of 0.5 $M_\odot$, 2.0 Gyr, and 0.2 dex, respectively, centered on the asteroseismic values for 94 Aqr Aa. When the rotation period is used as a constraint in the standard spin-down models, the relatively rapid rotation forces the fit to a higher mass of $1.27 \pm 0.02\ M_\odot$, substantially above the asteroseismic constraint ($1.22 \pm 0.02\ M_\odot$).

Although Aa is in a 6.3 year binary orbit, we do not expect the companion to affect the rotation period of the star. Binary companions closer than ~100 AU may affect the initial rotation period of a star by shortening the lifetime of the protostellar disk (Messina et al. 2017). However, this difference is present only in young systems, as the subsequent angular momentum evolution makes the periods in old stars insensitive to the initial conditions. As we have already discussed above, even if the star were to begin the main-sequence rotating at break-up, its rotation in the subgiant phase is minimally affected. The companion star is sufficiently distant that it is not expected to interact tidally, and even then it cannot cause tidal spin-up in its current configuration.

7. CONCLUSIONS AND DISCUSSION

By combining Mount Wilson observations of magnetic variability with asteroseismic measurements of the G8 subgiant 94 Aqr Aa from TESS, we have discovered new evidence for weakened magnetic braking (van Saders et al. 2016) and the possibility of a "born-again" dynamo in evolved stars (see below).

A reanalysis of 35 years of HK observations (Section 3) yields rotation and magnetic activity cycle periods for 94 Aqr Aa ($\mathrm{P}_{\mathrm{rot}}^{\mathrm{Aa}} = 46.69 \pm 3.66$ days, $\mathrm{P}_{\mathrm{cyc}}^{\mathrm{Aa}} = 19.35 \pm 0.18$ yr) and 94 Aqr B ($\mathrm{P}_{\mathrm{rot}}^{\mathrm{B}} = 38.90 \pm 1.93$ days, $\mathrm{P}_{\mathrm{cyc}}^{\mathrm{B}} = 9.13 \pm 0.03$ yr). The amplitude of the observed variability in the blended A component allows us to attribute these properties to the subgiant (Aa) because it contributes 97% of the light in the relevant bandpasses.

Asteroseismology of 94 Aqr Aa from TESS observations (Section 4) yields precise determinations of the stellar radius ($R = 2.06 \pm 0.05\ R_\odot$), mass ($M = 1.22 \pm 0.02\ M_\odot$) and age ($t = 6.2 \pm 0.4$ Gyr). We establish the absolute accuracy of these properties (Section 5) with independent estimates of the stellar radius from SED fitting ($R_{\mathrm{SED}} = 2.07 \pm 0.03\ R_\odot$), the stellar mass from a close binary orbit ($M_{\mathrm{Aa}} = 1.24 \pm 0.08\ M_\odot$), and the system age from gyrochronology of the K dwarf secondary ($t_{\mathrm{gyro}} = 6.3 \pm 0.6$ Gyr).

Using the asteroseismic properties from Section 4, we attempted to reproduce the observed rotation period from Section 3 with angular momentum evolution models (Section 6) that adopted either standard spin-down or the weakened magnetic braking proposed by van Saders et al. (2016). The standard model predicts a rotation period ($P = 78.0^{+6.0}_{-6.5}$ days) that is substantially longer than suggested by the observations, while the model with weakened magnetic braking ($P = 48.3^{+3.3}_{-3.6}$ days) naturally reproduces the observed rotation period with stalled spin-down at a critical Rossby number $\mathrm{Ro}_{crit} = 1.97$ (van Saders et al. 2019).

The fact that the G8 subgiant shows a magnetic activity cycle provides a strong constraint on stellar dynamo models. According to the scenario proposed by Metcalfe & van Saders (2017), activity cycles should gradually grow longer with the rotation period along the two sequences identified by Böhm-Vitense (2007). When a star reaches the critical Rossby number suggested by van Saders et al. (2016), the rotation period appears to stay relatively constant while the activity cycle grows longer and weaker before disappearing entirely. The resulting "flat activity" star still shows magnetic activity on small scales, allowing rotation periods to be measured, but the mean activity level is approximately constant on longer timescales. Such stars have previously been interpreted as Maunder minimum candidates (Judge et al. 2004), but at least some of them may actually be the end-states of large-scale stellar dynamos.

If the critical Rossby number represents a threshold above which large-scale dynamos no longer operate, then models with weakened magnetic braking may help to explain the existence of a cycle in 94 Aqr Aa. The mass of this G8 subgiant suggests that it evolved from an F-type star on the main-sequence. As such, it may have had a relatively short activity cycle until it reached the critical Rossby number after about 2.5 Gyr (see Figure 8) at a rotation period near 15 days (e.g., see Metcalfe et al. 2019, their Fig. 1). The cycle would then grow longer and weaker for more than 2 Gyr at nearly constant Rossby number. When hydrogen burning ceases, the core contracts and the star becomes hotter with a thinner convection zone, pushing it across Ro_{crit} and making it a "flat activity" star. However, the star subsequently expands and cools when hydrogen shell-burning begins, slowing its rotation through conservation of angular momentum and deepening the outer convection zone. For a small range of masses above the solar value, these evolutionary effects can push the Rossby number

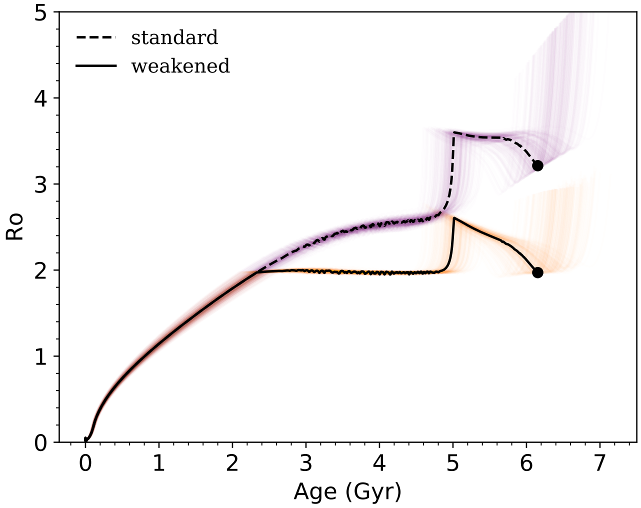

Figure 8. Predictions from a standard spin-down model (purple/dashed) and weakened braking model (orange/solid) for the evolution of the Rossby number in 94 Aqr Aa. For each model, the best-fit combination of mass and composition is shown as a dark line and the best fit age is marked with a solid point. In addition, 250 randomly drawn posterior samples of mass and composition are shown, truncated at the end of the subgiant branch.

back below Ro_{crit} (solid line in Figure 8) so the star can reinvigorate large-scale dynamo action and briefly sustain an activity cycle before ascending the red giant branch. This scenario for a "born-again" dynamo is simply not possible with standard spin-down models.

A similar mechanism may help explain the existence of magnetic cycles in subgiants that evolved from more massive F-type stars, which had never previously sustained a large-scale dynamo. For example, Egeland (2018) used Mount Wilson and Lowell observations to identify an activity cycle in the subgiant component of the HD 81809 system. The mass of this star ($1.58\pm0.26\ M_\odot$) would place it above the Kraft break on the main-sequence, without a substantial outer convection zone to help build a large-scale magnetic field. Consequently, it would not experience significant magnetic braking during its main-sequence lifetime, and it would only slow to its current rotation period (40.2 ± 2.3 days) through expansion on the subgiant branch. The deeper convection zone during this evolutionary phase could finally support large-scale dynamo action for the first time in its life, explaining the observed activity cycle.

The results presented above demonstrate the scientific potential of combining magnetic variability data from Mount Wilson and other programs with new asteroseismic observations from TESS. With precise and accurate determinations of the basic stellar properties such as radius, mass and age, we can finally make evolutionary connections between stars with known rotation rates and magnetic activity cycles. Over the coming years, this approach promises to yield additional insights about magnetic stellar evolution beyond the middle of main-sequence lifetimes.

ACKNOWLEDGMENTS

This work benefited from discussions within the international team "The Solar and Stellar Wind Connection: Heating processes and angular momentum loss" at the International Space Science Institute (ISSI). T.S.M. acknowledges support from NASA grants NNX16AB97G and 80NSSC20K0458, and from a Visiting Fellowship at the Max Planck Institute for Solar System Research. Computational time at the Texas Advanced Computing Center was provided through XSEDE allocation TG-AST090107.

REFERENCES

Adelberger, E. G., Austin, S. M., Bahcall, J. N., et al. 1998, Reviews of Modern Physics, 70, 1265, doi: 10.1103/RevModPhys.70.1265

Antia, H. M., & Basu, S. 1994, A&AS, 107, 421

Baliunas, S., Sokoloff, D., & Soon, W. 1996, ApJL, 457, L99, doi: 10.1086/309891

Baliunas, S. L., Hartmann, L., Noyes, R. W., et al. 1983, ApJ, 275, 752, doi: 10.1086/161572

Baliunas, S. L., Donahue, R. A., Soon, W. H., et al. 1995, ApJ, 438, 269, doi: 10.1086/175072

Ball, W. H., & Gizon, L. 2014, A&A, 568, A123

Barnes, S. A. 2010, ApJ, 722, 222, doi: 10.1088/0004-637X/722/1/222

Böhm-Vitense, E. 2007, ApJ, 657, 486, doi: 10.1086/510482

Brandenburg, A., Mathur, S., & Metcalfe, T. S. 2017, ApJ, 845, 79, doi: 10.3847/1538-4357/aa7cfa

Buzasi, D. L., Carboneau, L., Hessler, C., Lezcano, A., & Preston, H. 2015, in IAU General Assembly, Vol. 29, 2256843

Campante, T. L., Schofield, M., Kuszlewicz, J. S., et al. 2016, ApJ, 830, 138, doi: 10.3847/0004-637X/830/2/138

Casagrande, L., Portinari, L., Glass, I. S., et al. 2014, MNRAS, 439, 2060, doi: 10.1093/mnras/stu089

Christensen-Dalsgaard, J. 2008, Ap&SS, 316, 13, doi: 10.1007/s10509-007-9675-5

Creevey, O. L., Metcalfe, T. S., Schultheis, M., et al. 2017, A&A, 601, A67, doi: 10.1051/0004-6361/201629496

Deheuvels, S., & Michel, E. 2011, A&A, 535, A91, doi: 10.1051/0004-6361/201117232

Deheuvels, S., Doğan, G., Goupil, M. J., et al. 2014, A&A, 564, A27, doi: 10.1051/0004-6361/201322779

Demarque, P., Guenther, D. B., Li, L. H., Mazumdar, A., & Straka, C. W. 2008, Ap&SS, 316, 31, doi: 10.1007/s10509-007-9698-y

Denissenkov, P. A., Pinsonneault, M., Terndrup, D. M., & Newsham, G. 2010, ApJ, 716, 1269, doi: 10.1088/0004-637X/716/2/1269

Docobo, J. A., Tamazian, V. S., Campo, P. P., & Piccotti, L. 2018, AJ, 156, 85, doi: 10.3847/1538-3881/aad179

Donahue, R. A., Saar, S. H., & Baliunas, S. L. 1996, ApJ, 466, 384, doi: 10.1086/177517

Egeland, R. 2017, PhD thesis, Montana State University, Bozeman, Montana, USA

—. 2018, ApJ, 866, 80, doi: 10.3847/1538-4357/aadf86

Egeland, R., Soon, W., Baliunas, S., et al. 2017, ApJ, 835, doi: 10.3847/1538-4357/835/1/25

Fabricius, C., Høg, E., Makarov, V. V., et al. 2002, A&A, 384, 180, doi: 10.1051/0004-6361:20011822

Ferguson, J. W., Alexander, D. R., Allard, F., et al. 2005, ApJ, 623, 585, doi: 10.1086/428642

Foreman-Mackey, D., Hogg, D. W., Lang, D., & Goodman, J. 2013, PASP, 125, 306, doi: 10.1086/670067

Formicola, A., Imbriani, G., Costantini, H., et al. 2004, Physics Letters B, 591, 61, doi: 10.1016/j.physletb.2004.03.092

Fuhrmann, K. 2008, MNRAS, 384, 173, doi: 10.1111/j.1365-2966.2007.12671.x

Gaia Collaboration, Brown, A. G. A., Vallenari, A., et al. 2018, A&A, 616, A1, doi: 10.1051/0004-6361/201833051

Gray, R. O., Corbally, C. J., Garrison, R. F., et al. 2006, AJ, 132, 161, doi: 10.1086/504637

Grevesse, N., & Sauval, A. J. 1998, SSRv, 85, 161, doi: 10.1023/A:1005161325181

Hall, J. C., Lockwood, G. W., & Skiff, B. A. 2007, AJ, 133, 862, doi: 10.1086/510356

Harvey, J. W., Hill, F., Kennedy, J. R., Leibacher, J. W., & Livingston, W. C. 1988, Advances in Space Research, 8, 117, doi: 10.1016/0273-1177(88)90304-3

Iglesias, C. A., & Rogers, F. J. 1996, ApJ, 464, 943, doi: 10.1086/177381

Jenkins, J. M., Twicken, J. D., McCauliff, S., et al. 2016, in Proc. SPIE, Vol. 9913, Software and Cyberinfrastructure for Astronomy IV, 99133E

Judge, P. G., Saar, S. H., Carlsson, M., & Ayres, T. R. 2004, ApJ, 609, 392, doi: 10.1086/421044

Katoh, N., Itoh, Y., Toyota, E., & Sato, B. 2013, AJ, 145, 41, doi: 10.1088/0004-6256/145/2/41

Kraft, R. P. 1967, ApJ, 150, 551, doi: 10.1086/149359

Kurucz, R. L. 1992, in IAU Symposium, Vol. 149, The Stellar Populations of Galaxies, ed. B. Barbuy & A. Renzini, 225

Linsky, J. L., & Avrett, E. H. 1970, PASP, 82, 169, doi: 10.1086/128904

Lund, M. N., Handberg, R., Davies, G. R., Chaplin, W. J., & Jones, C. D. 2015, ApJ, 806, 30, doi: 10.1088/0004-637X/806/1/30

Lund, M. N., Handberg, R., Kjeldsen, H., Chaplin, W. J., & Christensen-Dalsgaard, J. 2017, in European Physical Journal Web of Conferences, Vol. 160, European Physical Journal Web of Conferences, 01005

MacGregor, K. B., & Brenner, M. 1991, ApJ, 376, 204, doi: 10.1086/170269

Marcadon, F., Appourchaux, T., & Marques, J. P. 2018, A&A, 617, A2, doi: 10.1051/0004-6361/201731628

Mason, B. D., Wycoff, G. L., Hartkopf, W. I., Douglass, G. G., & Worley, C. E. 2001, AJ, 122, 3466, doi: 10.1086/323920

Mermilliod, J. C. 2006, VizieR Online Data Catalog, II/168

Messina, S., Lanzafame, A. C., Malo, L., et al. 2017, A&A, 607, A3, doi: 10.1051/0004-6361/201730444

Metcalfe, T. S., Kochukhov, O., Ilyin, I. V., et al. 2019, ApJL, 887, L38, doi: 10.3847/2041-8213/ab5e48

Metcalfe, T. S., & van Saders, J. 2017, SoPh, 292, 126, doi: 10.1007/s11207-017-1157-5

Metcalfe, T. S., Monteiro, M. J. P. F. G., Thompson, M. J., et al. 2010, ApJ, 723, 1583, doi: 10.1088/0004-637X/723/2/1583

Montgomery, M. H., & O'Donoghue, D. 1999, Delta Scuti Star Newsletter, 13, 28

Mosser, B., Vrard, M., Belkacem, K., Deheuvels, S., & Goupil, M. J. 2015, A&A, 584, A50, doi: 10.1051/0004-6361/201527075

Paunzen, E. 2015, A&A, 580, A23, doi: 10.1051/0004-6361/201526413

Paxton, B., Bildsten, L., Dotter, A., et al. 2011, ApJS, 192, 3, doi: 10.1088/0067-0049/192/1/3

Ricker, G. R., Winn, J. N., Vanderspek, R., et al. 2014, in Society of Photo-Optical Instrumentation Engineers (SPIE) Conference Series, Vol. 9143, Proceedings of the SPIE, Volume 9143, id. 914320 15 pp. (2014)., 914320

Rogers, F. J., & Nayfonov, A. 2002, ApJ, 576, 1064, doi: 10.1086/341894

Sarma, M. B. K. 1962, ApJ, 135, 301, doi: 10.1086/147268

Serenelli, A., Johnson, J., Huber, D., et al. 2017, ApJS, 233, 23, doi: 10.3847/1538-4365/aa97df

Shibahashi, H. 1979, PASJ, 31, 87

Somers, G., & Pinsonneault, M. H. 2016, ApJ, 829, 32, doi: 10.3847/0004-637X/829/1/32

Soon, W. H., Baliunas, S. L., & Zhang, Q. 1994, SoPh, 154, 385, doi: 10.1007/BF00681107

Stassun, K. G., Collins, K. A., & Gaudi, B. S. 2017, AJ, 153, 136, doi: 10.3847/1538-3881/aa5df3

Stassun, K. G., Corsaro, E., Pepper, J. A., & Gaudi, B. S. 2018, AJ, 155, 22, doi: 10.3847/1538-3881/aa998a

Stassun, K. G., & Torres, G. 2016, ApJL, 831, L6, doi: 10.3847/2041-8205/831/1/L6

—. 2018, ApJ, 862, 61, doi: 10.3847/1538-4357/aacafc

Steigman, G. 2010, JCAP, 4, 029. https://arxiv.org/abs/1002.3604

Thoul, A. A., Bahcall, J. N., & Loeb, A. 1994, ApJ, 421, 828, doi: 10.1086/173695

Tokovinin, A., Mason, B. D., Hartkopf, W. I., Mendez, R. A., & Horch, E. P. 2015, AJ, 150, 50, doi: 10.1088/0004-6256/150/2/50

van Saders, J. L., Ceillier, T., Metcalfe, T. S., et al. 2016, Nature, 529, 181, doi: 10.1038/nature16168

van Saders, J. L., & Pinsonneault, M. H. 2013, ApJ, 776, 67, doi: 10.1088/0004-637X/776/2/67

van Saders, J. L., Pinsonneault, M. H., & Barbieri, M. 2019, ApJ, 872, 128, doi: 10.3847/1538-4357/aafafe

VandenBerg, D. A., & Clem, J. L. 2003, AJ, 126, 778, doi: 10.1086/376840

Vaughan, A. H., Preston, G. W., & Wilson, O. C. 1978, PASP, 90, 267, doi: 10.1086/130324

White, O. R., & Livingston, W. C. 1981, ApJ, 249, 798, doi: 10.1086/159338

White, T. R., Huber, D., Mann, A. W., et al. 2018, MNRAS, 477, 4403, doi: 10.1093/mnras/sty898

Wilson, O. C. 1978, ApJ, 226, 379, doi: 10.1086/156618

Zechmeister, M., & Kürster, M. 2009, A&A, 496, 577, doi: 10.1051/0004-6361:200811296

Zinn, J. C. 2019, in American Astronomical Society Meeting Abstracts, Vol. 233, American Astronomical Society Meeting Abstracts #233, 341.07